analytical chemistry

pubs.acs.org/ac Article

Biometric Photoelectrochemical–Visual Multimodal Biosensor Based on 3D Hollow HCdS@Au Nanospheres Coupled with Target-Induced Ion Exchange Reaction for Antigen Detection

Yuting Zhou,[†] Shuzhen Lv,[†] Xin-yan Wang, Lingyi Kong, and Sai Bi*

Cite This: *Anal. Chem.* 2022, 94, 14492–14501 Read Online

ACCESS | Metrics & More | Article Recommendations | Supporting Information

ABSTRACT: Three-dimensional (3D) hollow photoactive nanomaterials can enhance light capture due to the light scattering benefiting from the unique hollow nanostructures, which contributes to the decrease in energy loss and the electron–hole recombination during the process of photoelectric conversion. Herein, a 3D hollow HCdS@Au nanosphere synthesized by the templated-assisted method and photodeposition is employed to construct a multimodal sensing platform by combining the photoelectrochemical (PEC) biosensor with colorimetric analysis and photothermal imaging. In the presence of target carcinoembryonic antigen (CEA), a sandwich structure is formed on magnetic beads based on the dual-aptamer recognition, followed by the initiation of rolling circle amplification (RCA) to bind numerous CuO-DNA probes. Upon stimulation by chlorhydric acidic, a large number of Cu^{2+} is released from CuO, which could interact with yellow HCdS@Au on electrode to produce dark CuS by ion exchange. As a result, with increased CEA level, the photocurrent is weakened and the color of electrode interface is changed from yellow to dark, which thus facilitates the PEC and colorimetric detection of CEA. Simultaneously, the formed CuS with highly photothermal effect can achieve qualitative visual analysis of CEA using a portable infrared thermal imager. This work exhibits an excellent performance for sensitive and selective detection of CEA in the dynamic working range from 0.015 to 2.4 ng/mL with a detection limit as low as 3.5 pg/mL. Moreover, the proposed PEC biosensor is successfully applied to CEA determination in human serum, which holds great promise in accurate analysis of biomarkers and early diagnosis of diseases in the clinic.

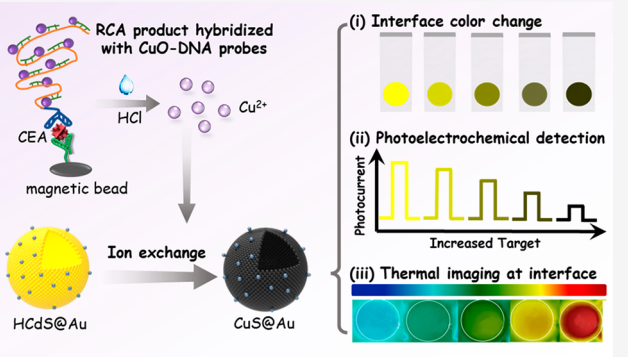

To meet the requirements of sensitivity, selectivity, portability, and rapid detection, a variety of regulating strategies have been proposed for enhancing the performance of biosensors in terms of interfacial design, signal amplification, and device construction. In particular, PEC biosensors with the advantages of high sensitivity, low cost, and great accuracy have become a kind of powerful and robust tool.[1] Determining the properties of light harvesting, charge separation and transport during the process of photoelectric conversion, and the photoactivity of nanomaterials play vital roles in interfacial design to improve the sensitivity of PEC biosensors.[2] The morphology control, element doping, and heterostructure construction are effective ways to obtain the photoactive materials with high photoelectric conversion efficiency.[3] Among these, nanostructure engineering in morphology control has demonstrated as an efficient strategy.[4,5] To date, zero dimensional (0D) quantum dots, one-dimensional (1D) nanowires/nanorods, two-dimensional (2D) nanosheets, and three-dimensional (3D) hollow nanostructures have been synthesized as photoactive nanomaterials with highly photoelectric conversion efficiency. Endowed with the tunable shell thickness, large surface area, and separate void space, the 3D hollow photoactive nanomaterials can enhance the light capture via light scattering.[6,7] The majority of energy loss in photoexcitation process results from the electron–hole recombination which is reduced by the hollow nanostructures. Therefore, employing 3D hollow photoactive nanomaterials to improve the analytical performance of PEC biosensors is promising.

Visual analysis in biosensors can transform biometric information triggered by the target into color change, possessing the advantages of real-time detection, low cost, and simple operation for the determination of various biomolecules.[8] The traditional visual analysis is mainly based on the color change induced by the aggregation or decomposition of noble metal nanoparticles, fluorescence switch, enzyme catalysis, and

Received: September 5, 2022
Accepted: September 28, 2022
Published: October 4, 2022

https://doi.org/10.1021/acs.analchem.2c03885
Anal. Chem. 2022, 94, 14492–14501

Scheme 1. Biometric Photoelectrochemical–Visual Multimodal Biosensor Based on 3D Hollow HCdS@Au Nanosphere Coupled with RCA and Target-Induced Ion Exchange Reaction

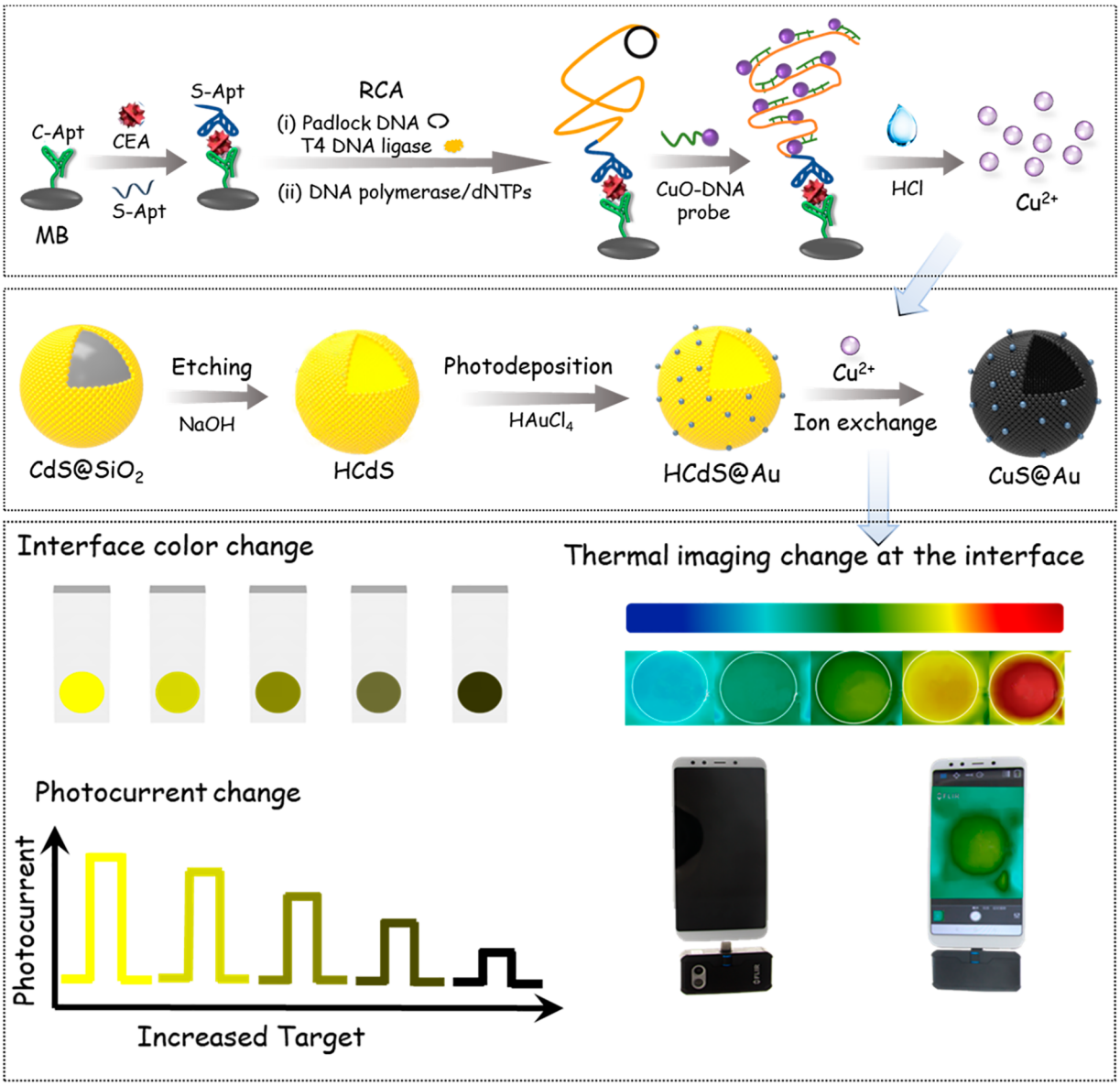

photonic crystals.[9,10] In recent years, optothermal nanomaterials, such as AuNPs, CuS, TMB, and titanium carbide MXene quantum dots (Ti_3C_2 MXene QDs), have been explored in thermal imaging or catalysis of chromogen for visual analysis. Owing to the easy operation, low cost, and great convenience in analysis, the photothermal systems with visual signal source in biosensors open a new horizon for versatile detection of disease biomarkers.

However, single mode detection often faces the challenges to improve the reliability and precision in quantitative determination. Therefore, multimodal analysis has attracted great attention in recent years. For example, PEC biosensors have combined with other electrochemical analytical techniques for biomarkers detection, such as electrochemiluminescent (ECL), differential pulse voltammetry (DPV), and chronoamperometry (CA),[11−13] which have turned into a new trend for achieving high accuracy and confidence level.[14] However, multimodal analysis merely based on the different electrochemical signal lacks portability and perceptual intuition. Therefore, it is highly desirable to construct more versatile multimode biosensing platforms.

In this work, we have combined PEC biosensor with visual analysis of colorimetric detection and photothermal imaging to construct a multimodal sensing platform on the basis of 3D hollow HCdS@Au nanospheres for the determination of CEA (Scheme 1). First, the solid CdS@SiO_2, synthesized from the in situ growth of CdS on the surface of SiO_2, is transformed into hollow CdS (HCdS) by template etching. Then, the HCdS is treated with photodeposition in $HAuCl_4$ solution to obtain the HCdS@Au. With the unique hollow nanostructures, HCdS@Au can enhance the light capture via light scattering, resulting in the improved photocurrent in comparison with the solid CdS@Au. Moreover, the Au NPs as the bridge can facilitate the photon-generated carrier transmission. For CEA detection, the "capture aptamer" (C-Apt) fixed on the magnetite beads (MBs) and the "signal aptamer" (S-Apt) with the primer sequence of

https://doi.org/10.1021/acs.analchem.2c03885
Anal. Chem. 2022, 94, 14492−14501

RCA can specifically recognize CEA. After magnetic separation, the linear padlock can be cyclized by the primer DNA with the assistance of T4 DNA ligase, followed by the initiation of RCA in the presence of phi29 DNA polymerase/dNTPs. As a result, large amounts of CuO-DNA probes can be hybridized with the repeated units of RCA products. Upon acidic stimulation, Cu^{2+} can be released from CuO, which further interacts with yellow HCdS@Au to produce dark CuS by ion exchange. As a result, with the increased CEA concentration, the photocurrent is weakened and the color of interface electrode is changed from yellow to dark. Meanwhile, owing to the high photothermal effect of the formed CuS,[15] the visual thermal imagery of electrode interface can be readily observed using a portable infrared thermal imager. Compared with other multimodal biosensors, this multimodal sensing platform with visual analysis possesses portability and perceptual intuition. In addition, the PEC mode could provide high sensitivity for target detection. Overall, through coupling 3D hollow HCdS@Au nanosphere with RCA and target-induced ion exchange, this work provides a new pathway for multimodal sensing with improved reliability, portability, and sensitivity, which is promising in the application of clinical diagnosis for biomarkers.

EXPERIMENTAL SECTION

Preparation of Hollow CdS (HCdS) Nanospheres. The SiO_2@CdS core−shell nanospheres were first prepared by an oil bath method according to the previous work.[16−18] First, 150 mg of SiO_2 nanospheres was dispersed in 100 mL of deionized water under ultrasound. Then, 1 mL of sodium citrate aqueous solution ($C_6H_5Na_3O_7·2H_2O$, 1 M) was added into the above solution before stirring for 10 min. Next, 0.5 mL of $CdCl_2$ solution (1 M) was added into the mixture dropwise. After stirring for another 10 min, 2 mL of ammonia ($NH_3·H_2O$, 28%) and 2 mL of thiourea solution (1 M) were slowly added into the above solution. The obtained well-distributed solution was transferred and heated in an oil bath at 80 °C for 3 h. The prepared SiO_2@CdS core−shell nanospheres were cooled to room temperature and washed with ethanol three times by centrifugation (9500 r/min). The purified SiO_2@CdS core−shell nanospheres were obtained via vacuum drying at 60 °C for 12 h.

For the preparation of HCdS nanospheres, the as-synthesized SiO_2@CdS core−shell nanospheres were put into 50 mL of NaOH solution (0.5 M) and heated at 90 °C for 3 h to remove the SiO_2 template. Finally, the synthetic HCdS nanosperes were washed with deionized water and ethanol until the pH of the supernatant was 7.0, followed by drying at 60 °C for 12 h in vacuum drying oven.

Preparation of HCdS@Au Nanospheres. The obtained HCdS nanospheres were put into 50 mL of deionized water with ultrasonic dispersion. Then, 200 μL of $HAuCl_4$ (1%) was introduced into the well-distributed HCdS suspension to carry out the photodeposition of Au (300 W xenon lamp) at 70 °C under magnetic stirring for 2 h. Afterward, the product was collected and washed by centrifugation (9500 r/min, 10 min) with deionized water and ethanol three times, respectively. Finally, the HCdS@Au nanospheres were obtained by vacuum drying at 60 °C for 12 h.

Conjugation of C-Apt on CMBs. First, 100 μL of carboxylated magnetic beads (CMBs) was thoroughly washed with MES buffer (0.01 M, pH 5.0) three times and then redispersed in 100 μL of MES buffer for further usage. Then, 200 μL of the mixed solution containing EDC (0.1 M) and NHS (0.01 M) was added into the above CMBs suspension and incubated at room temperature for 30 min to activate carboxyl groups on CMBs. The activated CMBs were washed with MES buffer three times and redispersed in 100 μL of PBS buffer (0.01 M, pH 7.4). Subsequently, 20 μL of amino-modified C-Apt was mixed with the activated CMBs and incubated for 12 h at 37 °C. The resulting C-Apt/CMBs conjugates were washed with PBS (0.01 M, pH 7.4) twice and redispersed in 120 μL of PBS (0.01 M, pH 7.4) before use.

Preparation of CuO-DNA Probes. First, the streptavidin (SA)-connected CuO was prepared according to the previous work.[19,20] In brief, 5 mg of CuO nanospheres with an average diameter of 40 nm was washed with deionized water three times and then dispersed in 1 mL of deionized water with ultrasound. Then, 20 μL of SA (1 mg mL^{-1}) and 50 μL of CuO suspension (5 mg mL^{-1}) were added into 430 μL of PBS (10 mM, pH 7.4) containing 0.1% Tween-20. After incubation at room temperature overnight, the mixture was centrifuged (7500 r/min) to remove the supernatant and washed three times with PBS (10 mM, pH 7.4). The obtained SA-coated CuO NPs (CuO-SA) was redispersed in 500 μL of PBS buffer (10 mM, pH 7.4) and stored at 4 °C for further usage. Then, 50 μL of biotin-modified S-Apt (20 μM) was added into the above mixture and incubated for 5 h at room temperature. After that, the formed CuO-DNA probes were washed with PBS three times by centrifugation (6000 r/min) and redispersed in 500 μL of PBS (10 mM, pH 7.4) for further usage.

Multimodel Sensing of CEA. The CEA at various concentrations was added into 100 μL of C-Apt/CMBs and incubated for 90 min at 37 °C to form the C-Apt/CMBs/CEA conjugates. Subsequently, 20 μL of S-Apt (10 μM) was added and incubated for 1 h to construct the sandwich structure. After washing with PBS (10 mM, pH 7.4) three times via magnetic separation and dispersed in 140 μL of PBS (10 mM, pH 7.4), 20 μL of padlock probe (10 μM) and 1 μL of T4 DNA ligase (1.25 U) dispersed in 1× T4 ligase reaction buffer (40 mM Tris-HCl, 10 mM $MgCl_2$, 10 mM DTT, 0.5 mM ATP, pH 7.8) were introduced, followed by incubation at 16 °C for 12 h. Then, the RCA reaction was executed after adding phi29 DNA polymerase (10 U) and dNTPs (10 mM) in 1× phi29 DNA polymerase buffer and reacted for 2 h. The resulting conjugates were washed three times with PBS (10 mM, pH 7.4) by magnetic separation, followed by adding 50 μL of CuO-DNA probes (0.5 mg mL^{-1}) and incubating at 30 °C for 2 h to make them hybridized with the RCA products. After washing with deionized water three times by magnetic separation, 30 μL of HCl (1 mM) was added and reacted with CuO to release Cu^{2+}.

The visual analysis was executed by the color changes of photoelectrode and the interface thermal imagery, respectively. The color of HCdS@Au nanospheres on photoelectrode changed from yellow to black with the increased CEA concentration based on the ion exchange reaction between the released Cu^{2+} and yellow HCdS@Au nanospheres, resulting in the generation of dark CuS. Furthermore, the photothermal images of the above photoelectrodes were recorded after irradiation by NIR laser (808 nm, 1.0 W) for 600 s.

Prior to PEC detection, the fluorine doped tin oxide (FTO) electrode was washed with absolute ethanol three times. A waterproof tape with a round hole (diameter of 6 mm, area of 28.26 mm^2) was affixed on the cleaned FTO electrode. Then, the photoelectrode was prepared by dropping HCdS@Au nanospheres (5 mg mL^{-1} dispersed in ultrapure water) on the hole and then naturally dried at room temperature. Then, the

https://doi.org/10.1021/acs.analchem.2c03885
Anal. Chem. 2022, 94, 14492−14501

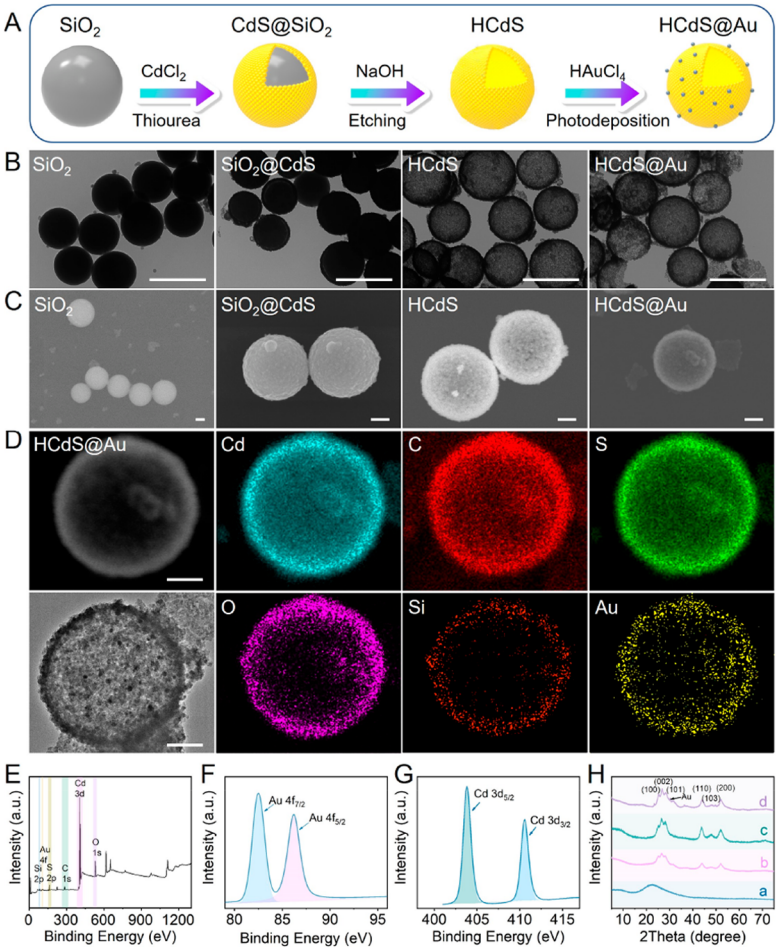

Figure 1. (A) Schematic illustration of HCdS@Au preparation process. (B) TEM images, (C) SEM images, and (D) EDS elemental mapping of SiO_2, SiO_2@CdS, HCdS, and HCdS@Au, respectively. Scale bars in (B) and (C) are 500 and 100 nm, respectively. (E) XPS survey spectrum of HCdS@Au. (F) High-resolution XPS spectra of Au 4f. (G) High-resolution XPS spectra of Cd 3d. (H) XRD patterns of (a) SiO_2, (b) SiO_2@CdS, (c) HCdS, and (d) HCdS@Au.

above released Cu^{2+} solution was dropped onto the photoelectrodes modified with HCdS@Au and incubated at room temperature for 20 min. After gently washing with deionized water, the PEC measurements were carried out on the device that combined a Xenon lamp (300 W) with electrochemical workstation (CHI 660E). The photocurrents as sensing signals relative to CEA concentration were recorded via a three-electrode system (FTO as working electrode, Ag/AgCl as reference electrode, and Pt wire as counter electrode) under $i-t$ mode. All PEC measurements were executed at room temperature unless other specified.

RESULTS AND DISCUSSION

Characterization of HCdS@Au Nanosphere. The HCdS nanospheres with dispersed AuNPs on the surface were prepared by the template-assisted method and photodeposition (Figure 1A). As the sacrificial template for the preparation of HCdS, the morphology of SiO_2 nanospheres was first characterized by scanning electron microscopy (SEM) and transmission electron microscopy (TEM), respectively. The SiO_2 nanospheres with an average diameter of 400 nm display good monodispersity and smooth surfaces (Figure 1B). After treatment with the facile low-temperature hydrothermal method, the CdS thin shell grows on the external surface of SiO_2 to acquire the solid SiO_2@CdS nanospheres (Figure 1C). Compared with the bare SiO_2 nanospheres with smooth surfaces, the surface of prepared SiO_2@CdS nanospheres becomes rougher. In addition, the high-angle annular dark field scanning transmission electron microscopy (HAADF-STEM) and energy dispersive spectrometer (EDS) elemental mapping prove the presence of cadmium (Cd) and sulfur (S) elements in SiO_2@CdS nanospheres (Figure 1D), which is consistent with the results of X-ray photoelectron spectroscopy (XPS) (Figure 1E,F). More detailed chemical information is obtained from the corresponding high-resolution XPS spectras of S 2p and Cd 3d. The peak at 161.5 eV corresponds to the S 2p and the peaks at 411.77 and 405.05 eV are attributed to Cd 3d, indicating the presence of CdS on SiO_2 surface.[21] Further, the crystalline phase of SiO_2@CdS nanospheres was further characterized by X-ray diffraction (XRD).[22] In contrast with the amorphous SiO_2, the XRD pattern of SiO_2@CdS possessing six typical diffraction peaks is in accordance with the planes of standard hexagonal CdS (JCPDS 80-0006) (Figure 1H).

After treatment with alkali etching to remove SiO_2 template in SiO_2@CdS nanospheres, the HCdS nanospheres were obtained. The morphology of etched SiO_2@CdS still remains a sphere, and the remaining CdS layer exhibits the hollow structure (Figure 1B,C). According to the HAAD-STEM and EDS elemental mapping (Figure 1D), the content of external Cd and S elements in HCdS still remains at a high level, while the Si

https://doi.org/10.1021/acs.analchem.2c03885
Anal. Chem. 2022, 94, 14492−14501

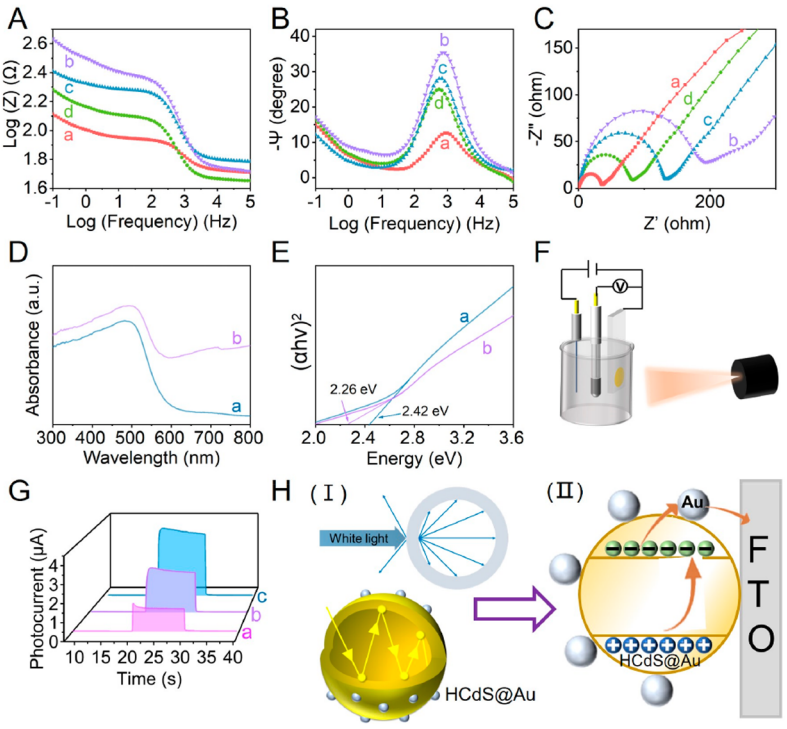

Figure 2. (A) Bode plots, (B) Bode phase angle plot, and (C) EIS measurements of Nyquist plot (a, bare electrode; b, SiO_2@CdS; c, HCdS; d, HCdS@Au). (D) UV−vis diffuse reflectance spectra and (E) Tauc plots of (a) HCdS and (b) HCdS@Au. (F) Schematic illustration of three-electrode system. (G) Photocurrent test of (a) SiO_2@CdS, (b) HCdS, and (c) HCdS@Au. (H) Illustration of (I) light scattering within the HCdS@Au hollow structure and (II) photoexcited charge-carrier distribution of HCdS@Au.

element obviously decreases in comparison with that of SiO_2@CdS, which is consistent with the results of XPS (Figure 1E). Moreover, according to XRD, there is no obvious change in CdS crystalline phase after etching the SiO_2 template of SiO_2@CdS (Figure 1H), which indicates the great crystal structure of the hollow HCdS.

Moreover, the HCdS@Au was obtained from the photodeposition of Au NPs on the surface of HCdS nanospheres. The hollow structure of CdS and the formation of AuNPs are significant to improve the photocurrent. According to TEM and SEM images (Figure 1B,C), the uniform Au NPs with a diameter of 10 nm can be readily observed on the surface of HCdS. The Au element also exists in STEM-EDS elemental mapping (Figure 1D) and XPS survey spectrum (Figure 1E). Notably, the high-resolution XPS spectra offers more detailed chemical information on the elements in HCdS@Au (Figure 1F,G). It is obvious that the Au 4f binding energies are centered at 83.6 eV ($4f_{7/2}$) and 87.2 eV ($4f_{5/2}$), which demonstrates the metallic state of Au.[23] The change of HCdS crystalline phase after the formation of HCdS@Au was proved by XRD (Figure 1H). The diffraction peaks of HCdS still exist and a new diffraction peak appearing at 38.2° is ascribed to the (110) plane of AuNPs according to JCPDS no. 01-089-3697.[24] These results demonstrate the monocrystalline state of the formed AuNPs and the successful synthesis of HCdS@Au.

Characterization of Photoelectrodes Performance. The photoelectrochemical properties of SiO_2@CdS, HCdS, and HCdS@Au coated onto FTO electrodes are investigated, respectively. The electrolyte interfacial resistance as well as the charge transfer resistance of photoelectrode interface are proved by the Bode plots obtained from the electrochemical impedance spectroscopy (EIS) measurements (5 mM $[Fe(CN)_6]^{3-/4-}$ as electrolyte; 10^5−10^{-2} Hz) under the illumination of xenon lamp (Figure 2A). The low-frequency region between 10^{-1} and 10^1 Hz reveals that the HCdS@Au-modified electrode possesses the fastest charge transfer compared with the SiO_2@CdS and HCdS-modified electrodes.[25] At the high frequency region, all electrodes display convergence ranging from $10^{1.5}$ to $10^{1.8}$, demonstrating the low electrolyte interfacial resistance. The shallow slope of HCdS@Au electrode in Bode plots also demonstrates a faster charge transfer ability than that of other photoactive nanomaterials with high slopes. A Bode phase angle plot against frequency is shown in Figure 2B. Compared with the SiO_2@CdS and HCdS electrodes, the maximum frequency of HCdS@Au electrode shifts to the low frequency region with the lowest phase angle, which indicates the lowest reaction resistivity between the electrolyte and electrode. In the Nyquist plot, the electron transfer resistance (R_{et}) is illustrated by the semicircle diameter at higher frequencies, whereas the diffusion process is represented by the linear component at lower frequencies.[26,27] As shown in Figure 2C, the diameter of HCdS@Au electrode is the smallest among all electrodes, which indicates the best conductivity owing to the high electron transmittability of AuNPs and the improved light absorption. The UV−vis diffuse reflectance spectra (DRS) further demonstrates that AuNPs play an important role in promoting the light absorption of HCdS (Figure 2D). It is noteworthy that HCdS exhibits a strong light absorption with an absorption edge at 480 nm. When AuNPs are generated on the surface of HCdS, the absorption edge of HCdS@Au displays a red shift in comparison with HCdS, which indicates the contribution of Au NPs to promote the light absorption. The band gap of the samples is estimated by transforming the light absorption spectra into Tauc plots (Figure 2E) and calculated by eq 1:

https://doi.org/10.1021/acs.analchem.2c03885
Anal. Chem. 2022, 94, 14492−14501

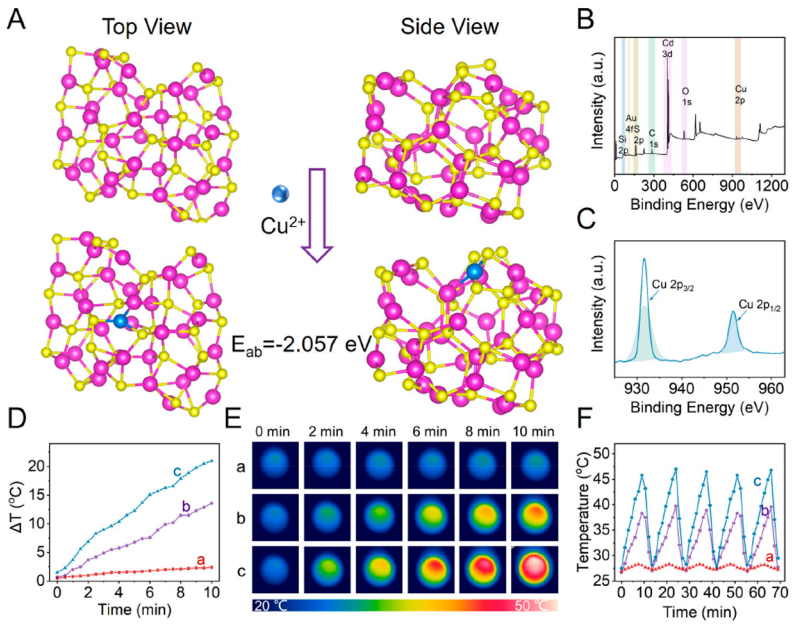

Figure 3. (A) Structures of $Cd_{33}S_{33}$ cluster and its reaction with Cu^{2+} ion (Cd, S, and Cu atoms are colored in purple, yellow, and blue, respectively). (B) XPS survey spectrum and (C) high-resolution spectrum of HCdS@Au after reacting with Cu^{2+}. (D) Temperature changes of (a) HCdS@Au, (b) CuS:HCdS@Au (1:1), and (c) CuS under NIR laser (808 nm, 1.5 W/cm^2). (E) Photothermal diagram and (F) thermostability of (a) HCdS@Au, (b) CuS/HCdS@Au (1:1), and (c) CuS.

$$\alpha h\nu = A(h\nu - E_g)^{1/2} \quad (1)$$

where α represents the absorption coefficient; E_g represents the band gap; ν represents the light frequency; A represents the proportional constant; h represents the Planck constant.[28] The band gaps of HCdS and HCdS@Au deduced from the intercept of tangent are calculated to be 2.42 and 2.26 eV, respectively. The photocurrents of different photoelectrodes were tested under on−off light irradiation with a three-electrode system (Figure 2F). As expected, the HCdS photoelectrode shows a considerable improvement in the photocurrent compared with SiO_2@CdS modified photoelectrode due to the multiple light scattering of 3D hollow nanostructures of CdS (Figure 2G,H). Moreover, the HCdS@Au exhibits a higher photocurrent intensity compared with the HCdS and SiO_2@CdS modified photoelectrodes because AuNPs on the surface of HCdS boost the transfer efficiency of photogenerated electron.[29]

Characterization of RCA Process. In this work, the RCA reaction is employed for signal amplification, which plays an important role in improving the sensing performance. In brief, the linear padlock DNA that hybridizes with the primer sequence on S-Apt is circularized by T4 DNA ligase to form the circular template, and then the RCA reaction is triggered in the presence of phi29 DNA polymerase/dNTPs, generating long single-stranded DNAs with a large number of repetitive sequences for the hybridization with CuO-DNA probes.[30] The nondenaturing polyacrylamide gel electrophoresis (PAGE) was executed to verify the process of RCA (Figure S1A). Compared with the linear padlock DNA (lane 2), a band with slower migration is produced after the interaction between padlock DNA and primer in S-Apt with the assistance of T4 DNA ligase (lane 4), indicating the successful circularization of linear padlock DNA.[31] The remaining bands are speculated to be the unreacted linear padlock DNA and the byproducts generated when the circular template is formed. Upon the introduction of phi29 DNA polymerase/dNTPs, the RCA reaction is initiated, and a bright band is observed at the initial position of PAGE (lane 5), indicating the slow fluidity of the obtained RCA products. As expected, after hybridization of DNA probes, the resulting products with large molecular weight are generated (lane 6).

In addition, as the signal source, CuO-DNA probes are critical for the construction of the multimodal biosensor. Here, the CuO nanoparticles (NPs) modified with SA via the electrostatic interaction are characterized by dynamic light scattering (DLS). As shown in Figure S1B, the CuO NPs demonstrate a diameter of ∼40 nm. After connection with SA, the diameter increases to ∼65 nm. Then, the biotin-modified DNAs link with CuO NPs by the specific interaction between SA and biotin to form the CuO-DNA probes, and the diameter is further increased to ∼98 nm. Similarly, the diameter of C-Apt/MBs is also characterized by DLS, which is larger than that of bare MBs, demonstrating the successful synthesis of C-Apt/MBs (Figure S1C) and laying a good foundation for signal amplification.

Characterization of Ion Exchange. To explore and interpret the ion-exchange processes, it is necessary to establish the models to understand and predict the extent of ion-exchange reaction under given conditions. Density functional theory (DFT) calculation was employed to demonstrate the strong binding affinity between CdS and Cu^{2+} ions in this reaction using $Cd_{33}S_{33}$ cluster as a model (Figure 3A). The largest adsorption energy for Cu^{2+} on $Cd_{33}S_{33}$ is calculated to be −2.057 eV from DFT, indicating that Cu^{2+} ions could carry out chemisorption on $Cd_{33}S_{33}$ and the ion exchange reaction can occur for the formation of CuS. Further, the binding force of Cu−S bond is stronger than that of Cd−S bond, while the K_{sp} of CuS is lower than that of CdS. The formation of CuS creates a new center of electron−hole recombination, thus generating the trapping sites located on the surface of CdS and impeding the formation of exciton to block the escape of photoelectron and decrease the photocurrent.[32,33] Furthermore, the formed CuS was analyzed by XPS (Figure 3B). Besides the peaks

https://doi.org/10.1021/acs.analchem.2c03885
Anal. Chem. 2022, 94, 14492−14501

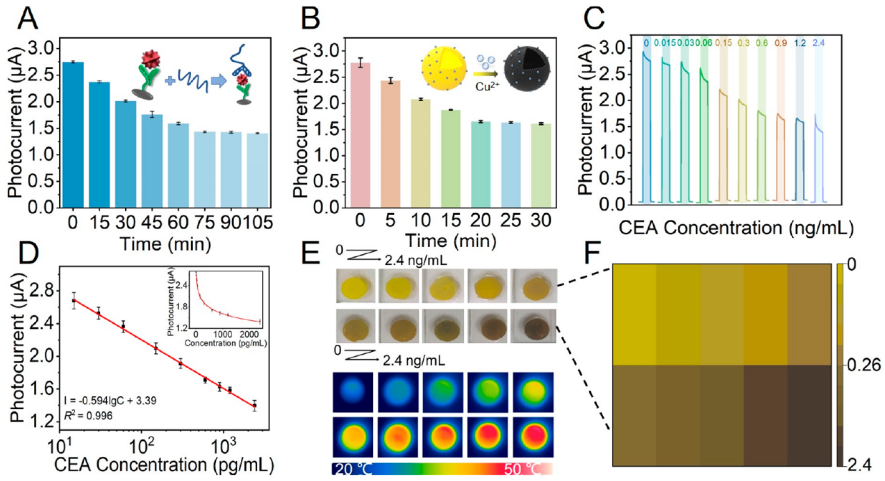

Figure 4. Optimization of (A) incubation time of S-Apt with CEA and (B) reaction time of ion exchange. (C) Photocurrents of the proposed PEC biosensor toward CEA standards with different concentrations (0, 0.015, 0.03, 0.06 0.15, 0.3, 0.6, 0.9 1.2, and 2.4 ng/mL) in 0.2 M Na_2SO_4. (D) Corresponding calibration curve derived from (C). (E) Color changes (top) and photothermal images (bottom) of photoelectrode interfaces toward CEA standards with different concentrations (0, 0.015, 0.03, 0.06, 0.15, 0.3, 0.6, 0.9, 1.2, and 2.4 ng/mL). (F) Color chart of photoelectrode interface toward different CEA concentrations in (E).

corresponding to Au, S, and Cd elements, the peak of Cu element appears. From the high-resolution XPS spectra of Cu 2p (Figure 3C), the binding energies at 931.9 and 951.8 eV are ascribed to Cu $2p_{3/2}$ and Cu $2p_{1/2}$, respectively, further confirming the formation of CuS.

As the results of ion exchange, the formed CuS can be employed as excellent photothermal materials. Figure 3D shows the evolution of temperature change ($\Delta T = T - T_0$, where T and T_0 represent the final and initial temperatures, respectively) of different photoactive nanomaterials on photoelectrode interface under NIR laser irradiation (808 nm, 1.5 W/cm^2). The HCdS@Au photoelectrode interface exhibits a weak temperature variation as the test time increased owing to the poor photothermal characteristic of HCdS and the tiny amount of AuNPs. In contrast, the CuS/HCdS@Au photoelectrode interface displays a rapid temperature rise due to the great photothermal property. However, the final temperature of the CuS/HCdS@Au photoelectrode interface is lower than that of CuS photoelectrode interface owing to the concentration-dependent photothermal effect. The photothermal images of these photoelectrodes are captured by a portable infrared thermal imager at 600 s, which shows that the photothermal effect of the photoelectrode interface is strongly concentration-dependent (Figure 3E). Thus, the different colors of thermal imagery can be clearly distinguished with the increased CuS proportion. To explore the photothermal stability of photoelectrode interfaces, five alternately "on−off" cycles were carried out. Satisfactorily, all the photoelectrode interfaces, including CuS, HCdS@Au, and CuS/HCdS@Au, exhibit the stable photothermal switching behavior (Figure 3F). Similar to the CuS photoelectrode, the CuS/HCdS@Au photoelectrode interface possesses nearly identical NIR response in every cycle, thus laying a good foundation for visual photothermal imaging.

Optimization of Conditions. To obtain the best analytical performance and detection efficiency, some important conditions have been optimized using the proposed PEC biosensor, such as the incubation time of S-Apt and CEA, as well as the reaction time between Cu^{2+} and HCdS@Au for ion exchange. The specific dual-aptamer recognition (C-Apt and S-Apt) for target CEA occurs on MBs. In particular, the incubation time between S-Apt and CEA is significant, which is related to the following RCA reaction and further influence the photocurrent responses. As shown in Figure 4A, with the incubation time increased, the photocurrent decreases accordingly, which tends to be flat after 75 min. A longer incubation time has no significant effect on photocurrent. Therefore, the optimal incubation time of S-Apt and CEA for constructing this biosensor is chosen as 75 min. In addition, the photocurrent is dependent on the reaction time of ion exchange between Cu^{2+} and HCdS@Au. As shown in Figure 4B, the photocurrent decreases with increasing reaction time and almost exhibits a plateau after 20 min. To ensure sufficient reaction and obtain the best analytical performance, the reaction time between Cu^{2+} and HCdS@Au is selected as 20 min.

Analytical Performance of Photochemical−Visual Biosensor for CEA Detection. Under the optimal experimental conditions, the established photochemical−visual sensing platform was employed to detect CEA with various concentrations. As shown in Figure 4C, the photocurrents of this PEC biosensor decrease with the increased CEA concentration. When the concentration of CEA ranges from 0.015 to 2.4 ng mL^{-1}, a good linear relationship is obtained between the photocurrent and the logarithm of CEA concentration (Figure 4D). The detection limit is calculated as 3.5 pg/mL, which is lower or comparable to the reported PEC, electrochemical and fluorescent biosensors (Table S2). Meanwhile, based on the ion exchange reaction, the color change of the photoelectrode interface with increased CEA concentration can be clearly observed from yellow CdS to dark CuS (Figure 4E,F). Moreover, as excellent optothermal material, the formed CuS has a high photothermal conversion efficiency. Using a portable infrared thermal imager, the photothermal visual tests were carried out. As shown in Figure 4E, the temperatures of photoelectrode interfaces increase with increased CEA concentrations, resulting in a visual photothermal imagery.

Selectivity, Reproducibility, and Stability. To investigate the selectivity of this PEC biosensor, several disease-related biomolecules in human blood, such as bovine albumin (BSA), glucose oxidase (GOx), exosome (EXO), were selected

https://doi.org/10.1021/acs.analchem.2c03885
Anal. Chem. 2022, 94, 14492−14501

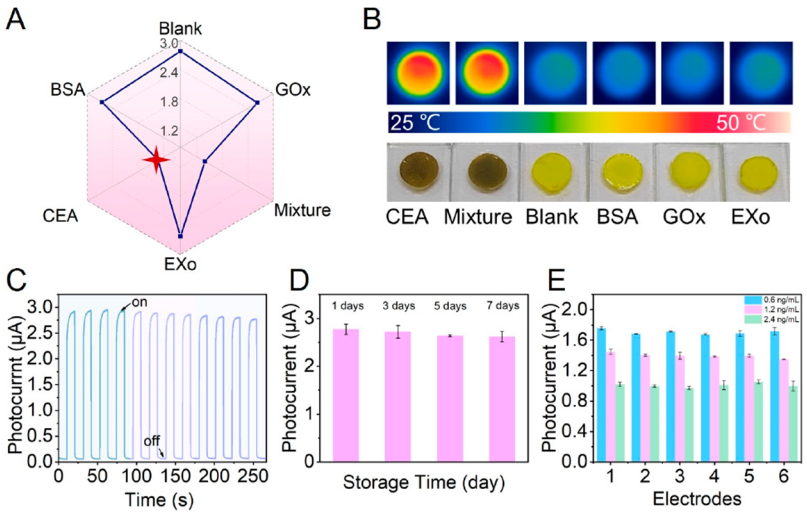

Figure 5. (A) Specificity of the proposed PEC biosensor toward different analytes. The concentration of target CEA is 2.0 ng mL^{-1}, while the concentrations of nontarget analytes are 10 ng mL^{-1} (mixture contained CEA and nontarget analytes). (B) Specificity of the visual biosensors for different analytes: photothermal images (top) and color change (bottom) of the photoelectrode interface. (C) Stability of HCdS@Au-modified FTO electrode. (D) Photocurrents of HCdS@Au-modified FTO electrodes after storage for 1, 3, 5, and 7 days. (E) Photocurrents of six equally prepared HCdS@Au-modified FTO electrodes for target CEA detection with the concentrations of 0.6, 1.2, and 2.4 ng mL^{-1}.

as the interfering analytes. The concentration of these interferents was 10 ng mL^{-1}. As shown in Figure 5A, the nontarget molecules even with the concentration 5-fold higher than that of target CEA only generate relatively low photocurrent responses, which are basically consistent with that of the blank group. Nevertheless, the groups of pure CEA or CEA-containing mixture can trigger significant signal changes, which demonstrates the prominent selectivity of the proposed PEC biosensor to distinguish target CEA from the interferents. The results of the corresponding visual analysis of the electrode interface are shown in Figure 5B.

The outputting steady photocurrent by the photoelectrode lays the foundation for the good stability and reproducibility of the PEC biosensor.[34] Hence, the sustaining photocurrent tests of HCdS@Au photoelectrode were carried out under "on−off" irradiation of the xenon lamp (Figure 5C). For the photocurrents of 12 times alternately "on−off" cycles, the obtained repeated photocurrent responses display a convergence.

The relative standard deviation (RSD) values of these photocurrents are 98.5% (on) and 99.8% (off) (n = 12), respectively, demonstrating the great stability of HCdS@Au photoelectrode in terms of photocurrent output. In addition, the storage stability of the HCdS@Au photoelectrode has been investigated (Figure 5D). The five parallel HCdS@Au photoelectrodes were stored for 0, 1, 3, 5, and 7 days at room temperature, respectively. After storage for 7 days, the photocurrent of the HCdS@Au photoelectrode remains 94.5% of the initial response, which indicates the good storage stability of the HCdS@Au photoelectrodes. To investigate the reproducibility of this PEC biosensor, six independent biosensors were prepared in parallel by the same method for the determination of CEA at 0.6, 1.2, and 2.4 ng mL^{-1}, respectively. As shown in Figure 5E, the photocurrents of these six photoelectrodes are almost at the same level with the same concentration of CEA. The RSD values of the PEC biosensor toward 0.6, 1.2, and 2.4 ng mL^{-1} CEA are 2.00%, 2.13%, and 3.52%, respectively, which proves the good repeatability of this biosensing platform.[35]

Real Sample Analysis. To verify the practical potential applications of the proposed PEC biosensor, different concentrations of CEA were added into the 100-fold diluted human serum, achieving the recoveries of 93.4−102.8% with the RSD less than 5% (Table 1). The corresponding visual analysis results of these electrode interfaces are shown in Figure S2. All the results prove the good practicability of the established photochemical−visual biosensor for CEA detection in complex biological environments, which is practical to sensitive and selective analysis of CEA in clinical applications.

Table 1. Determination of CEA in 100-Fold Diluted Human Serum by Standard Addition Method Using the Proposed PEC Biosensor

sample	added (ng/mL)	found (ng/mL)	RSD (n = 3, %)	recovery (%)
1	0	0.0120	3.20	
2	0.05	0.0467	5.00	93.4
3	0.1	0.0936	1.12	93.6
4	1.0	0.9850	2.88	98.5
5	2.0	2.0560	1.46	102.8

CONCLUSION

In summary, this work has constructed a multimodal sensing platform through integrating PEC with visual analysis (colorimetry and photothermal imaging) based on 3D hollow HCdS@Au coupled with target-triggered RCA and ion exchange for amplified detection of CEA. The hollow HCdS with tunable shell thickness, large surface area, and separate void space has high light-capture capacity due to the light scattering, thus contributing to a higher photocurrent response in comparison with the solid CdS. The Au NPs on hollow CdS with high electroconductibility give rise to the hot electron generation and contribute to the photoinduced charge separation, which is beneficial to further improvement of photocurrent response. Moreover, the signal amplification accomplished by RCA significantly improves the detection sensitivity. Based on the multirole hollow HCdS@Au for ion exchange, the multimode

https://doi.org/10.1021/acs.analchem.2c03885
Anal. Chem. 2022, 94, 14492−14501

analysis of CEA is accomplished by PEC and visual analysis (colorimetry and photothermal imaging). On one hand, the PEC mode of this multimodal sensing platform provides high sensitivity. On the other hand, the visual analysis achieves great reliability and perceptual intuition. This biosensor is also successfully applied to the detection of CEA in human serum samples. Overall, the proposed multimodal biosensing platform opens a promising avenue for biomarkers detection and displays the potential applications in clinical diagnosis.

■ ASSOCIATED CONTENT

Supporting Information

The Supporting Information is available free of charge at https://pubs.acs.org/doi/10.1021/acs.analchem.2c03885.

Additional experimental details, including materials and chemicals, and density functional theory (DFT) calculation; additional figures and tables, including non-denaturing PAGE characterization of RCA, DLS results, photothermal images and color change of the photoelectrode interface corresponding to the standard addition method, and comparison of various methods for CEA detection (PDF)

■ AUTHOR INFORMATION

Corresponding Author

Sai Bi − *College of Chemistry and Chemical Engineering, Qingdao University, Qingdao 266071, P. R. China;* orcid.org/0000-0002-7305-8233; Email: bisai11@126.com

Authors

Yuting Zhou − *College of Chemistry and Chemical Engineering, Qingdao University, Qingdao 266071, P. R. China*

Shuzhen Lv − *College of Chemistry and Chemical Engineering, Qingdao University, Qingdao 266071, P. R. China*

Xin-yan Wang − *College of Chemistry and Chemical Engineering, Qingdao University, Qingdao 266071, P. R. China*

Lingyi Kong − *College of Chemistry and Chemical Engineering, Qingdao University, Qingdao 266071, P. R. China*

Complete contact information is available at: https://pubs.acs.org/10.1021/acs.analchem.2c03885

Author Contributions

†Y.Z. and S.L. contributed equally. All authors have given approval to the final version of the manuscript.

Notes

The authors declare no competing financial interest.

■ ACKNOWLEDGMENTS

The authors acknowledge financial support from the National Natural Science Foundation of China (Grants 22076087 and 22104069), the Natural Science Foundation of Shandong Province (Grants ZR2020JQ08 and ZR2021QB057), and the Youth Innovation Technology Program of Shandong Province (Grant 2019KJC029).

■ REFERENCES

(1) Zhao, W. W.; Xu, J. J.; Chen, H. Y. *Chem. Rev.* **2014**, *114*, 7421−7441.

(2) Yu, Z.; Gong, H.; Xu, J.; Li, Y.; Zeng, Y.; Liu, X.; Tang, D. *Anal. Chem.* **2022**, *94*, 3418−3426.

(3) Huang, L.; Cai, G.; Zeng, R.; Yu, Z.; Tang, D. *Anal. Chem.* **2022**, *94*, 9487−9495.

(4) Zhu, W.; Chen, Z.; Pan, Y.; Dai, R.; Wu, Y.; Zhuang, Z.; Wang, D.; Peng, Q.; Chen, C.; Li, Y. *Adv. Mater.* **2019**, *31*, 1800426.

(5) Deng, J.; Su, Y.; Liu, D.; Yang, P.; Liu, B.; Liu, C. *Chem. Rev.* **2019**, *119*, 9221−9259.

(6) Xiao, M.; Wang, Z.; Lyu, M.; Luo, B.; Wang, S.; Liu, G.; Cheng, H. M.; Wang, L. *Adv. Mater.* **2019**, *31*, 1801369.

(7) Li, J.; Jia, S.; Sui, G.; Du, L.; Li, B. *RSC. Adv.* **2017**, *7*, 34857−34865.

(8) Fu, G.; Sanjay, S. T.; Zhou, W.; Brekken, R. A.; Kirken, R. A.; Li, X. *Anal. Chem.* **2018**, *90*, 5930−5937.

(9) Yang, T.; Luo, Z.; Tian, Y.; Qian, C.; Duan, Y. *TrAC-Trend Anal Chem.* **2020**, *124*, 115795.

(10) Chen, M.; Liu, Z.; Guan, Y.; Chen, Y.; Liu, W.; Liu, Y. *Sens. Actu., B* **2022**, *359*, 131609.

(11) He, Y.; Liu, Y.; Cheng, L.; Yang, Y.; Qiu, B.; Guo, L.; Wang, Y.; Lin, Z.; Hong, G. *ACS Appl. Mater. Interfaces* **2021**, *13*, 298−305.

(12) Kong, L.; Lv, S.; Qiao, Z.; Yan, Y.; Zhang, J.; Bi, S. *Biosens. Bioelectron.* **2022**, *207*, 114188.

(13) Wang, J.; Zhang, K.; Xu, H.; Yan, B.; Gao, F.; Shi, Y.; Du, Y. *Sens. Actu. B* **2018**, *276*, 322−330.

(14) Hai, X.; Li, Y.; Zhu, C.; Song, W.; Cao, J.; Bi, S. *TrAC-Trend Anal Chem.* **2020**, *133*, 116098.

(15) Lv, R.; Yang, P.; Hu, B.; Xu, J.; Shang, W.; Tian, J. *ACS Nano* **2017**, *11*, 1064−1072.

(16) Bie, C.; Zhu, B.; Xu, F.; Zhang, L.; Yu, J. *Adv. Mater.* **2019**, *31*, 1902868.

(17) Zeng, R.; Wang, W.; Cai, G.; Huang, Z.; Tao, J.; Tang, D.; Zhu, C. *Nano Energy* **2020**, *74*, 104931.

(18) Wu, X.; Zhang, H.; Dong, J.; Qiu, M.; Kong, J.; Zhang, Y.; Li, Y.; Xu, G.; Zhang, J.; Ye, J. *Nano Energy* **2018**, *45*, 109−117.

(19) Qu, W.; Liu, Y.; Liu, D.; Wang, Z.; Jiang, X. *Angew. Chem., Int. Ed. Engl.* **2011**, *50*, 3442−3445.

(20) Yang, Z.; Yi, C.; Lv, S.; Sheng, Y.; Wen, W.; Zhang, X.; Wang, S. *Sens. Actu. B* **2019**, *285*, 326−332.

(21) Zhu, N.; Tang, J.; Tang, C.; Duan, P.; Yao, L.; Wu, Y.; Dionysiou, D. D. *Chem. Eng. J.* **2018**, *353*, 237−245.

(22) Sun, G.; Zhang, Y.; Kong, Q.; Zheng, X.; Yu, J.; Song, X. *Biosens. Bioelectron.* **2015**, *66*, 565−571.

(23) Lv, S.; Zhang, K.; Zeng, Y.; Tang, D. *Anal. Chem.* **2018**, *90*, 7086−7093.

(24) An, L.; Cao, M.; Zhang, X.; Lin, J.; Tian, Q.; Yang, S. *ACS Appl. Mater. Interfaces* **2020**, *12*, 8050−8061.

(25) Wei, Z. Q.; Hou, S.; Lin, X.; Xu, S.; Dai, X. C.; Li, Y. H.; Li, J. Y.; Xiao, F. X.; Xu, Y. J. *J. Am. Chem. Soc.* **2020**, *142*, 21899−21912.

(26) Qin, Y.; Wen, J.; Zheng, L.; Yan, H.; Jiao, L.; Wang, X.; Cai, X.; Wu, Y.; Chen, G.; Chen, L.; Hu, L.; Gu, W.; Zhu, C. *Nano Lett.* **2021**, *21*, 1879−1887.

(27) Shen, Q.; Han, L.; Fan, G.; Zhang, J. R.; Jiang, L.; Zhu, J. J. *Anal. Chem.* **2015**, *87*, 4949−4956.

(28) Bi, Q.; Dang, C.; Wang, Z.; Zhang, Z.; Wu, G.; Cheng, W.; Xue, J. *Appl. Surf. Sci.* **2021**, *541*, 148688.

(29) Gao, Y.; Zeng, Y.; Liu, X.; Tang, D. *Anal. Chem.* **2022**, *94*, 4859−4865.

(30) Liu, J.; Jin, J.; Deng, Z.; Huang, S. Z.; Hu, Z. Y.; Wang, L.; Wang, C.; Chen, L. H.; Li, Y.; Van Tendeloo, G.; Su, B. L. *J. Colloid Interface Sci.* **2012**, *384*, 1−9.

(31) Ge, J.; Hu, Y.; Deng, R.; Li, Z.; Zhang, K.; Shi, M.; Yang, D.; Cai, R.; Tan, W. *Anal. Chem.* **2020**, *92*, 13588−13594.

(32) Liu, Y.-W.; Ko, D.-K.; Oh, S. J.; Gordon, T. R.; Doan-Nguyen, V.; Paik, T.; Kang, Y.; Ye, X.; Jin, L.; Kagan, C. R.; Murray, C. B. *Chem. Mater.* **2011**, *23*, 4657−4659.

(33) Zelaya-Angel, O.; Garcia-Rocha, M.; Mendoza-Alvarez, J. G.; Cardenas, M.; Aguilar-Hernandez, J. *J. Appl. Phys.* **2003**, *94*, 2284−2288.

(34) Zeng, R.; Gong, H.; Li, Y.; Li, Y.; Lin, W.; Tang, D.; Knopp, D. *Anal. Chem.* **2022**, *94*, 7442−7448.

(35) Zeng, R.; Wang, W.; Chen, M.; Wan, Q.; Wang, C.; Knopp, D.; Tang, D. *Nano Energy* **2021**, *82*, 105711.

https://doi.org/10.1021/acs.analchem.2c03885
Anal. Chem. 2022, 94, 14492−14501